2026 IEEE International Conference on Robotics and Automation (ICRA 2026)
June 1-5, 2026. Vienna, Austria

Augmenting the Reach: Visualizing Robotic Working Volume at the Tool Tip for Intuitive Retinal Access in Eye Surgery.

Junjie Yang[1], Satoshi Inagaki[1], Zhihao Zhao[1], Daniel Zapp[2], Kai Huang[3], M. Ali Nasseri[2]

***Abstract*— Retinal Surgery Robotics is a rapidly emerging field that offers enhanced precision by overcoming human tremors. A key trend of these robotic designs is toward more compact and lightweight structures for improved positioning accuracy and precise force delivery. However, this compactness sacrifices the robot's working volume, making it difficult for ophthalmic surgeons to intuitively assess if retinal targets are accessible by the surgical tool tip. This paper proposes a methodology for visualizing the actual accessible area in the microscopic view to provide surgeons with an intuitive visual guide of the tool's reach, reducing uncertainty and streamlining extraocular robotic maneuvers. We validated this method on a commercial phantom with a surgical robot system, achieving $\leqslant$1.0 deg error for 83.3% of tested points across four retinal subareas and demonstrating its clinical potential.**

I. INTRODUCTION

Ophthalmic robotics has emerged as a revolutionary participant in surgical techniques [1]. For instance, in the challenging task of subretinal injection where even expert surgeons have a success rate of 50% or less [2], robotic assistance has been shown in simulations [3] and ex vivo experiments [4] to significantly enhance manipulation at the delicate 10-100 micron scale [5]. Such high precision of surgical robots critically relies on their optimized physical dimensions and weight. More compact robotic structures can inherently reduce mechanical vibrations and increase maneuverability in constrained surgical spaces, enabling higher accuracy during instrument positioning. Furthermore, lighter robotic mechanisms enable more sensitive and precise force control, which is essential for delicate surgical interactions with tissue. Therefore, surgical robots are being compacted continuously in size and weight to enhance positioning accuracy and force precision.

However, such design optimization inevitably requires trade-offs, particularly by sacrificing the robot's maximum working volume and limiting its achievable force boundaries. Consider the Remote Center of Motion (RCM) constraint of a surgical tool pivoting around the trocar shown in Fig. 1, which aims at minimizing unexpected over-stretching to the sclera tissue. Once the tool is inserted through the trocar,

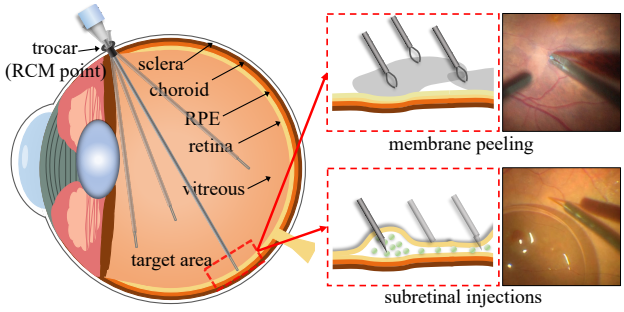

Fig. 1: Multi-target surgical tasks within limited areas in minimally invasive posterior-segment interventions.

the effective surgical workspace becomes the intersection of the visible area within the microscope's field of view and the robot's reachable volume. Since the design compactness has already reduced the surgical tool's working volume, the resulting tool tip's retinal working area is further narrowed significantly. Therefore, a critical challenge for existing robotic systems is ensuring that this limited accessible area can fully cover all the intended surgical targets on the retina.

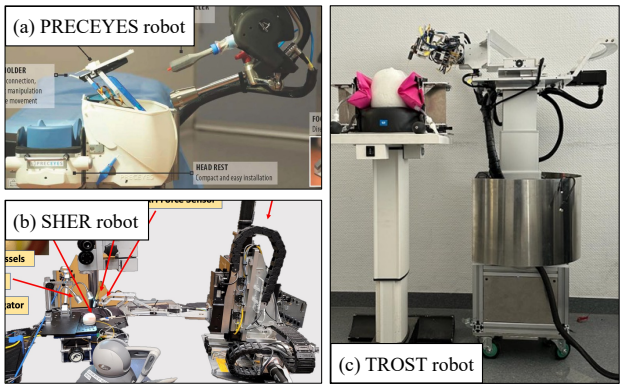

Fig. 2: Examples of compact robot systems for ophthalmic surgery. (a) PRECEYES [6] and (b) SHER [7] are fixed systems where extraocular alignment consumes a portion of the single manipulator's working volume. (c) TROST [8] is a mobile system that decouples these tasks using dedicated kinematics, preserving the intraocular manipulator's full working volume for surgery.

Some researchers use off-the-shelf arm systems, such as [6], [9], [10], to cover the whole posterior-segment area in ophthalmic applications with huge space-consuming cascaded links as a trade-off. Other ophthalmic surgical systems, such as [7], fix their compact robot structures beside the patient and rely on an appropriate allocation of working volume for the same kinematic structure to guarantee precise

This work is supported by state of Bavaria through Bayerische Forschungsstiftung (BFS) under Grant AZ-1592-23-ForNeRo.

[1]Technische Universität München, 80333 München, Germany {junjie.yang,satoshi.inagaki,zhihao.zhao}@tum.de
[2]Klinik und Poliklinik für Augenheilkunde, Klinikum rechts der Isar, 81675 München, Germany {daniel.zapp,ali.nasseri}@mri.tum.de
[3]Sun Yat-Sen University, 510006 Guangzhou, China huangk36@mail.sysu.edu.cn

This paper has undergone AI-assisted proofreading only to enhance readability.

extraocular tool-trocar docking and sufficient intraocular retina area coverage. In contrast, mobile systems, such as TROST [8], use a multi-step decoupled localization kinematics to 1) use the cart to localize the setup on the patient; 2) use a 4-DOF platform to localize the micromanipulator on the eye and through the trocar; 3) use a 5-DOF micromanipulator to localize the surgical tool inside the eye. Such designs of dedicated kinematics can preserve the full working volume of the micro-manipulator for surgery, but introduce their own complexities in coordination and setup.

Besides compact robots' hardware design, the precise placement of the limited working volume is critical to ensuring retinal accessibility. Although researchers have focused on preoperative planning systems that theoretically optimize tool manipulation [11], overly strict assumptions regarding ideal robot-to-eyeball coordinate calibration cause significant discrepancies between theoretical calculations and actual retinal accessibility. Moreover, accurately quantifying these deviations from extraocular eyeball coordinate models remains challenging, complicating assessments of whether robot reconfiguration could effectively enhance coverage of the targeted retinal area.

To address these challenges, a novel visualization method is introduced in this paper to directly display the robot's working volume at the instrument tip. By indicating actual retinal coverage in microscopic images, this visualization enables intuitive assessment of the robot's 3D working volume through real-time 2D visual feedback. After establishing the extraocular configuration to set the tool's working volume placement, the instrument is inserted axially until its point of retinal contact is approximated using shadow-based visual cues. Then, the conical working volume of the robot-controlled instrument is visualized by displaying the boundary points outlining the reachable area on the retina. With this explicit area visualization in the microscopic image, the robotic control system and surgeons can perform additional extraocular reconfiguring to ensure optimal accessibility to the targeted retinal area. The performance of our proposed method is evaluated using an ophthalmic robotic surgical system by assessing boundary-point accessibility on an eye phantom with realistic geometry and deformability.

The proposed area-boundary visualization method proves high effectiveness, correctly predicting intraocular accessibility for 83.3% of the 48 tested points across four retinal subareas with working-angle error within the range of [0, 1.5] degrees. Specifically, 25% of the points fell within the conservatively predefined working volume ($\leqslant 0^\circ$ error), while a further 58.3% were confirmed to be reachable with an acceptable deviation of less than 1.0°. Crucially, the visualization also identifies the remaining 16.7% of points as unexpectedly inaccessible in the current configuration (¿1° error). By validating reach and flagging inaccessibility, the proposed method provides direct and actionable feedback for surgeons to refine the robot's configuration to ensure complete target coverage.

The main contributions of this paper are as follows: **1)** A task flow for visualizing the valid tool–retina interaction area is proposed, enabling intuitive assessment of retinal accessibility. **2)** Experimental validation is performed using an eye-surgery robotic system to evaluate the effectiveness of the proposed retina coverage visualization method. **3)** An analysis of trocar-induced errors concerning area visualization is provided as a supplementary investigation to support experimental findings.

II. PREREQUISITES

A. 2D-3D Mapping

The proposed method requires the mutual mapping between 2D pixels from the microscope image and the 3D surface of the eyeball model after the microscope-eyeball alignment, keeping the eyeball static during surgeries. As shown in Fig. 3, this mapping is an ideal direct geometric projection, where a scaling factor relates pixel coordinates from a centered microscope view to a 3D spherical coordinate system. This geometrical mapping, defined as the function $p^{3d}_{obj} = g(p^{img}_{obj})$, is achieved by Equation (1).

$$\begin{aligned} x^{3d} &= (y^{img} - y^{img}_{center}) \cdot \sigma_{2d\to 3d} \\ y^{3d} &= (x^{img} - x^{img}_{center}) \cdot \sigma_{2d\to 3d} \\ z^{3d} &= \sqrt{(r_{eye})^2 - (x^{3d})^2 - (y^{3d})^2} \cdot \rho_p \end{aligned} \tag{1}$$

The 2D-3D scaling ratio $\sigma_{2d\to 3d} = d^{mm}_{limbus} \;/\; d^{pixel}_{limbus}$ is obtained by measuring and comparing the limbus diameters in the image (d^{pixel}_{limbus}) and in the 3D space (d^{mm}_{limbus} measured during preoperative diagnosis or the intraoperative trocar-placement phase). Noticeably, $\sigma_{2d\to 3d}$ can be updated from the real-time pixel distances of two trocars utilizing the RCM decomposition in [12] to tolerate microscope magnification. r_{eye}=12.0 mm is the eyeball radius. $\rho_p = \pm 1$ defines a point's location on the eye's upper or lower half.

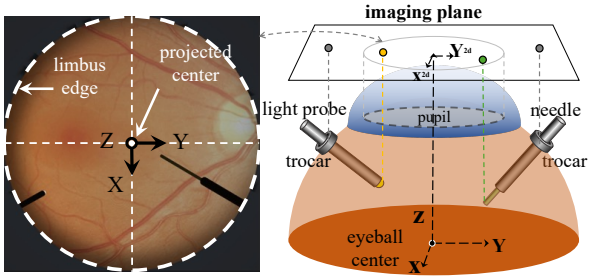

Fig. 3: Mutual 2D-3D mapping between eyeball and images.

However, in a clinical setting, this simple projection is significantly complicated by optical distortion introduced by the eye's anatomical structures [13], particularly the cornea and lens [14], [15]. Therefore, a comprehensive mapping must include a patient-specific undistortion model, $\mathbf{M}_{undist}$, to correct the pixel locations before the geometric projection, as shown conceptually in Equation (2).

$$\begin{aligned} p^{pixel,undist}_{obj} &= f_{undist}(p^{pixel}_{obj}, \mathbf{M}_{undist}) \\ p^{3d,undist}_{obj} &= g(p^{pixel,undist}_{obj}) \end{aligned} \tag{2}$$

Obtaining the parameters for $\mathbf{M}_{undist}$ requires an intact optical pathway for calibration. Since this study is conducted

on a lensless ophthalmic phantom with a realistic geometry, the optical calibration is infeasible. Therefore, we decouple the challenge of visualizing the robot's kinematic workspace from the separate and significant challenge of real-time optical undistortion. Hence, the direct geometric projection model is adopted, effectively treating p_{obj}^{pixel} and $p_{obj}^{pixel,undist}$ as equivalent, which is a necessary and standard simplification for phantom-based validation of robotic surgical systems.

B. Conic Working Volume

As shown in Fig. 2, compact eye-surgery robots are designed to move surgical tools with Remote Center of Motion (RCM) control, where the tool pivots around a fixed point to minimize tissue trauma [7], [16], [17], [18]. In the context of this work, the RCM point is considered to be the trocar entry location, which determines the tool's insertion axis as the local Z-axis. Consequently, the working volume is explored by rotating the tool around the local X and Y axes. Software-defined RCM systems may suffer from link bending and tip deviation due to gravity, which has been observed in long-link serial-parallel structures [11], [19]. To mitigate these effects, the robot's initial configuration is often designed to center target retinal points within the working volume to enhance motor precision. The consequent approximate equality of the X and Y-axis rotation angles allows us to simplify modeling the tool's working volume, representing it as a maximal symmetric cone, as shown in Fig. 4. Such symmetric simplification is critical for the proposed visualization method, which relies on defining the tool's orientation $\vec{v}_{axis}^{now}$ with a single working-angle parameter θ_{wv} rather than specifying the full 3D direction around the trocar. Nevertheless, the impact of neglecting the partial working volume outside this cone must be considered if corner retinal targets are required.

In this paper, the robot arm is initially configured such that its insertion axis, aligned with the surgical tool, defines the reference axis $\vec{v}_{axis}^{ref}$. Then, the current working angle θ_{wv} represents the extent to which the tool axis $\vec{v}_{axis}^{now}$ has been rotated away from the reference, as calculated by Equation (3).

$$\theta_{wv} = \text{acos}\left(\frac{\vec{v}_{axis}^{now} \cdot \vec{v}_{axis}^{ref}}{\|\vec{v}_{axis}^{now}\| \cdot \|\vec{v}_{axis}^{ref}\|}\right) \tag{3}$$

Additionally, the robot's hardware structure defines two limits: the maximal working angle θ_{wv}^{max}, and the RCM insertion length $d_{rcm} \in [0, d_{rcm}^{max}]$ defined as the distance from the trocar to the tool tip measured by motor encoders. For practical application, d_{rcm}^{max} must be greater than the eyeball diameter to ensure retinal accessibility.

Finally, the 3D working volume of the surgical tool $\mathcal{V}_{tool}^{3d}$ is defined as the set of all reachable tool tip points, p_{tool}^{3d}. Each point is calculated by starting at the 3D trocar point p_{rcm}^{3d}, and extending along a valid tool axis $\vec{v}_{axis}$ by the current RCM insertion length, d_{rcm}. A valid tool axis is any vector within the set $\mathbf{V}_{axis}$, which contains all possible orientations generated by rotating the initial reference axis $\vec{v}_{axis}^{ref}$ by any working angle θ_{wv} up to the hardware limit θ_{wv}^{max} as expressed in Equation (4).

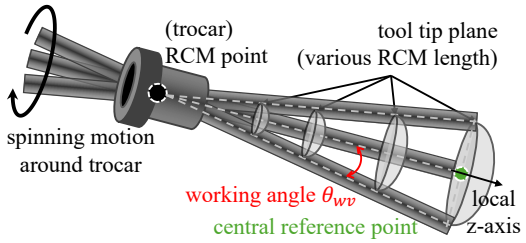

Fig. 4: Conic working-volume definition of cylinder-shaped surgical tools under the trocar-based RCM constraint.

$$\begin{aligned} \mathcal{V}_{tool}^{3d} &= \{p_{rcm}^{3d} + \vec{v}_{axis} \cdot d_{rcm} \mid \vec{v}_{axis} \in \mathbf{V}_{axis}\} \\ \text{where} \quad \mathbf{V}_{axis} &= \{\text{rotate}(\vec{v}_{axis}^{ref}, \theta_{wv}) \mid \theta_{wv} \in [0, \theta_{wv}^{max}]\} \end{aligned} \tag{4}$$

Since the trocar point p_{rcm}^{3d} is known after installation, and both d_{rcm} and θ_{wv}^{max} are parameters of the robot hardware, the entire 3D working volume's orientation is determined solely by the initial reference axis, $\vec{v}_{axis}^{ref}$.

III. METHOD

The overall task flow of the proposed working-area marking method is divided into three major stages for a static eye: preparation, extraocular configuration, and intraocular visualization, as presented in Fig. 5. Largely changed eye status will require a new round of extra-/intraocular configuration.

A. Preparation

The workflow begins with the standard surgical procedure where surgeons install trocars (typically three for infusion, tool, and a light probe) close to the limbus on the sclera. For accurate 2D-3D calculation, surgical assistants should align the microscope with the eyeball center, which is a practice fully compatible with the current OR setup. Once the trocars are in place, their 3D positions p_{rcm}^{3d} are determined using the 2D-3D mapping model $g(\cdot)$ explained in Equation (1) based on their identified pixel coordinates in the microscope image.

Finally, any preoperatively defined surgical targets are identified in the microscope image to create a target point set $\mathcal{P}_{tar}^{img} = \{p_{tar}^{img,i}, i \in [0, k)\}$, which will be used for the subsequent accessibility analysis.

B. Extraocular Stage Configuration

This stage involves two-step robot positioning with different precisions. First, the robot system is brought close to the patient's eye at decimeter precision. Then, an extraocular configuration procedure is performed to dock the tool tip precisely at the trocar entry point [20] at millimeter precision. Consequently, the tool's initial insertion axis ($\vec{v}_{axis}^{ref}$) and the initial placement of the working volume on the retina are determined.

The impact of this docking procedure on the available intraocular workspace depends on the robot's kinematic design.

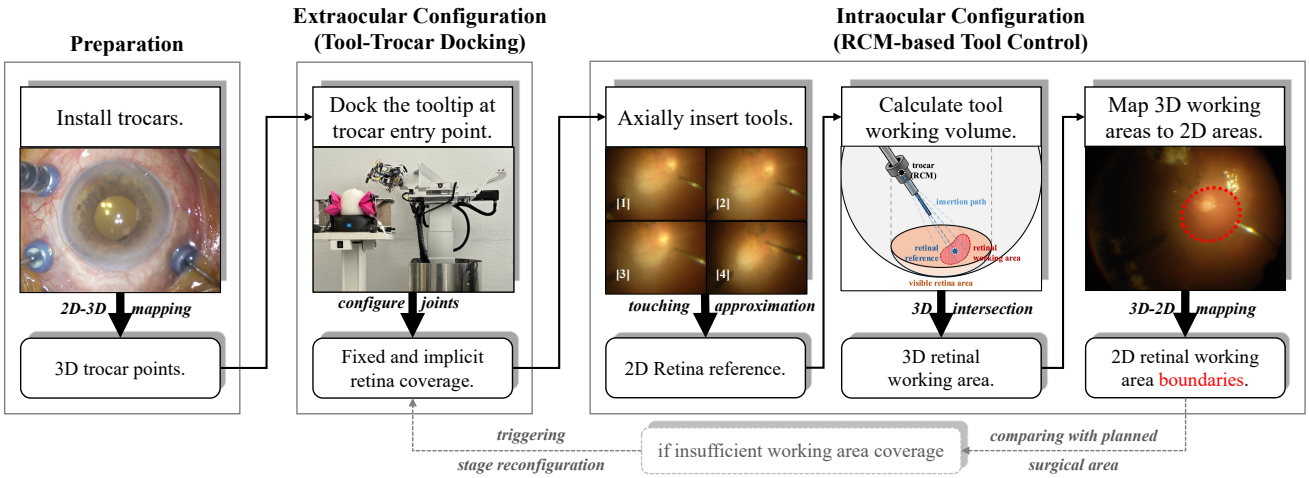

Fig. 5: The three-stage task flow for working area visualization. (a) Trocar localization; (b) Extraocular robot-tool docking to establish the RCM pivot; (c) Intraocular control and projection of the accessible retinal area onto the microscope image.

For systems with an integrated extra-intraocular configuration (e.g., [7]), the tool-trocar alignment consumes a portion of the manipulator's motion range, decreasing intraocular working volume. In contrast, the separated configuration used in this work [8] allows the mobile base stage to perform the tip-trocar docking and change the orientation of the conic working volume without reducing its maximal angle θ_{wv}^{max}. After this configuration is complete, the base stage remains static, and the system is ready for the intraocular visualization stage with a fully preserved working volume.

C. Intraocular Tool Control

1) T: o define the working volume using Equation (4), it is essential to first obtain the initial 3D reference orientation $\vec{v}_{axis}^{ref}$. This orientation $\vec{v}_{axis}^{ref}$ is defined by the fixed RCM trocar point p_{rcm}^{3d} and any other point p_{tool}^{3d} along the tool central axis, as shown in Equation (5).

$$\vec{v}_{axis}^{ref} = (p_{tool}^{3d} - p_{rcm}^{3d}) \;/\; \|p_{tool}^{3d} - p_{rcm}^{3d}\| \tag{5}$$

However, the tool tip p_{tip}^{3d} is floating within the vitreous humor after initial insertion, while the mapping function $g(\cdot)$ is only valid for on-surface points.

Our solution is to identify a retinal reference point that lies along the tool's insertion path. Specifically, we employ a shadow-based visual servoing technique, inspired by prior work of shadow utilization [21], [10], [22], to use the tool's shadow as a safe proxy for proximity to the retina. The tool is inserted axially while maintaining its initial orientation until the pixel distance between the tool tip p_{tip}^{img} and the shadow tip p_{shadow}^{img} decreases to a predefined threshold σ_{close}. At this point, the 2D touch point p_{touch}^{img} is approximated as the intersection of the tool's and shadow's orientation vectors in the image. Then, this 2D point is mapped to the 3D retinal surface, as described in Equation (6).

$$\begin{aligned} &\text{Given } \|p_{tip}^{img} - p_{shadow}^{img}\| \approx \sigma_{close}, \\ &p_{touch}^{img} = \text{intersect}((p_{tip}^{img}, \vec{v}_{axis}^{img}), (p_{shadow}^{img}, \vec{v}_{shadow}^{img})) \\ &p_{touch}^{3d} = g(p_{touch}^{img}) \end{aligned} \tag{6}$$

With the 3D touch point p_{touch}^{3d} robustly determined, the initial reference orientation $\vec{v}_{axis}^{ref}$ can be calculated using this point p_{touch}^{3d} and the known RCM point p_{rcm}^{3d} as per Equation (5).

We acknowledge that robust real-time shadow segmentation in microscopic imagery can be challenging due to variable illumination conditions. However, recent work has shown that state-of-the-art deep learning networks can reliably extract tool and shadow features for proximity estimation [21], [23], [24], which is sufficient for the retina surgery application in this paper.

*2) **Volume Calculation**:* With the initial orientation $\vec{v}_{axis}^{ref}$ now established, the next step is to calculate the boundary of the accessible retinal area $\mathcal{A}_{wv}$. This area is the intersection of the tool's conic working volume with the spherical surface of the eyeball $\mathcal{E}$ with its boundary a continuous curve $\mathcal{B}_{wv}$. For visualization, we approximate this continuous curve with a discrete set of N boundary points $\mathcal{B}_{wv}^{'}$ by a two-step procedure, as shown in Fig. 6.

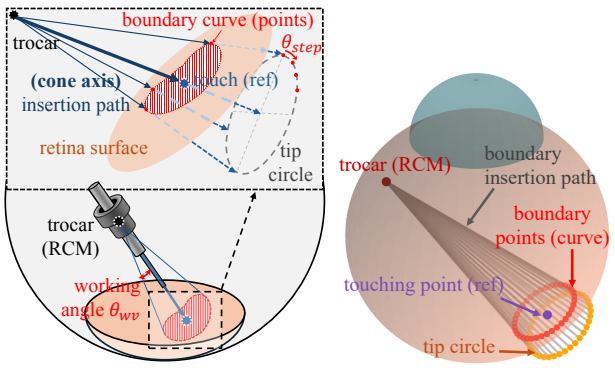

(a) Definition of working area. (b) 3D working volume.

Fig. 6: Figure (a) shows the retinal working-area generation in the 3D space with given parameters p_{rcm}^{3d}, d_{rcm}, $\vec{v}_{axis}^{ref}$ and θ_{wv}^{max}. Figure (b) is an example of volume generation.

Step-1: Generate the First Boundary Point. First, we calculate a single point on the boundary by finding the

intersection of the eyeball surface $\mathcal{E}$ with a tool orientation vector that is at the maximal working angle θ_{wv}^{max} from the reference axis. To generate a consistent starting vector, we rotate $\vec{v}_{axis}^{ref}$ by θ_{wv}^{max} towards the global up direction (Z-axis $\vec{v}_z$) within the plane defined by $\vec{v}_z$ and $\vec{v}_{axis}^{ref}$.

The calculation for this rotation is detailed in Equation (7). The geometric intuition is as follows. First, we find the angle between the reference vector and the XY-plane ($\theta_{axis\to XY}$). Then, we subtract the maximal working angle from this to find the target angle of our new vector relative to the XY-plane ($\theta_{calc\to XY}$). Finally, using this new angle and the original XY components of the reference vector, we calculate the new Z-component (z_{calc}) and re-normalize to get the final unit vector, $\vec{v}_{axis}^{calc}$.

$$
\begin{aligned}
\vec{v}_{axis\to XY}^{ref} &= \frac{[\vec{v}_{axis}^{ref}.x,\ \vec{v}_{axis}^{ref}.y,\ 0]^T}{\sqrt{(\vec{v}_{axis}^{ref}.x)^2 + (\vec{v}_{axis}^{ref}.y)^2}} \\
\theta_{axis\to XY} &= \text{acos}\left(\frac{\vec{v}_{axis\to XY}^{ref} \cdot \vec{v}_{axis}^{ref}}{\|\vec{v}_{axis\to XY}^{ref}\| \cdot \|\vec{v}_{axis}^{ref}\|}\right) \\
\theta_{calc\to XY} &= \theta_{axis\to XY} - \theta_{wv}^{max} \\
x_{calc} &= \vec{v}_{axis}^{ref}.x,\ y_{calc} = \vec{v}_{axis}^{ref}.y \\
\text{denoting } \alpha &= x_{calc}^2 + y_{calc}^2, \\
z_{calc} &= -\sqrt{\left(\frac{\alpha}{\sqrt{\alpha}\cdot\cos(\theta_{calc\to XY})}\right)^2 - \alpha} \\
\vec{v}_{axis}^{calc} &= \frac{[x_{calc}, y_{calc}, z_{calc}]^T}{\sqrt{x_{calc}^2 + y_{calc}^2 + z_{calc}^2}}
\end{aligned}
\tag{7}
$$

Step-2: Generate Remaining Points by Rotation. Obtaining the starting boundary vector $\vec{v}_{axis}^{calc}$, the remaining $N-1$ boundary vectors are generated by incrementally rotating $\vec{v}_{axis}^{calc}$ around the central conic axis $\vec{v}_{axis}^{ref}$ by a step angle, θ_{step}. For each resulting vector $\vec{v}_{axis}^{i}$, its intersection with the eyeball surface $\mathcal{E}$ gives a 3D boundary point $p_{boundary}^{3d,i}$, as formalized in Equation (8).

$$
\begin{aligned}
\mathcal{B}'_{wv} &= \{p_{boundary}^{3d,i} \mid i \in [0, N-1]\} \\
\text{where}\quad p_{boundary}^{3d,i} &= \text{intersect}(\vec{v}_{axis}^{i}, \mathcal{E}) \\
\text{and}\quad \vec{v}_{axis}^{i} &= \text{RotMatrix}(\vec{v}_{axis}^{ref}, i \cdot \theta_{step}) \cdot \vec{v}_{axis}^{calc}
\end{aligned}
\tag{8}
$$

This procedure results in a discrete set of 3D points $\mathcal{B}'_{wv}$ that effectively represents the boundary of the accessible retinal working area for the current robot configuration. To ensure the intersection is always found, these calculations use a virtual insertion length d_{rcm}^{calc} that is greater than the eyeball diameter (e.g., 24mm), making the calculation independent of the tool's actual depth.

*3) **Visualization**:* The final step is to project the calculated 3D boundary points $\mathcal{B}'_{wv}$ back onto the 2D microscope image to provide a real-time visual overlay for the surgeon. Each 3D point $p_{boundary}^{3d,i} \in \mathcal{B}'_{wv}$ lies on the retinal surface. Therefore, we can apply the inverse of our mapping function $g(\cdot)$ to project these points back into the image plane, creating a set of 2D boundary pixels $\mathcal{B}_{wv}^{img'}$.

$$
\begin{aligned}
\mathcal{B}_{wv}^{img'} &= \{p_{wv}^{img,i} \mid i \in [0, N-1]\} \\
\text{where}\quad p_{wv}^{img,i} &= g^{-1}(p_{boundary}^{3d,i})
\end{aligned}
\tag{9}
$$

Once these pixels are rendered as a contour on the live microscope feed, the visualization provides immediate and intuitive feedback. Surgeons can instantly assess whether the current robotic configuration provides adequate coverage for all preoperative targets and can confidently select new intra-operative targets, knowing they lie within an accessibility-guaranteed boundary.

D. Coverage Verification and Reconfiguration

This subsection describes the procedure for verifying target accessibility and guiding robotic reconfiguration if necessary. The workflow leverages two key pieces of information: the target point set $\mathcal{P}_{tar}^{img}$ obtained during *Preparation*, and the current working area boundary $\mathcal{B}'_{wv}$ calculated by the *Volume Calculation* steps.

*1) **Coverage Verification**:* First, we simply check to determine if all target points lie within the currently visualized accessible area. Each target point $p_{tar}^{img,i} \in \mathcal{P}_{tar}^{img}$ is compared against the boundary polygon formed by $\mathcal{B}'_{wv}$. If all points are inside, the current robot configuration is validated, and the surgeon can proceed with the intervention.

*2) **Reconfiguration Guidance**:* Extraocular robot reconfiguration is required if one or more target points lie outside the current boundary. The system calculates an ideal new reference point to assist the surgeon with reconfiguration. The goal is to find the new reference touch point p_{ideal}^{img} that allows the new working volume to cover all targets with the minimum possible extent. This ideal point is calculated as the center of the minimum enclosing circle containing all target points in $\mathcal{P}_{tar}^{img}$.

Once p_{ideal}^{img} is calculated, it is displayed on the microscope image. The system then instructs the surgeon to axially withdraw the tool, reconfigure the robot's base stage, and re-perform the *Finding Reference* procedure to align the new touch point with the displayed ideal point p_{ideal}^{img}. Consequently, this process provides a closed-loop and intuitive method for ensuring complete retinal coverage.

IV. EXPERIMENT

A. Setup

This paper uses a mobile eye-surgery robot system [8] to test the performance of retinal working-area generation. This robot system in Fig. 7 is composed of two parts: a 4-DoF base stage (three Cartesian translational and one rotational joint) and a 5-DoF robot arm (three Cartesian translational and two virtual rotational joints).

During eye surgeries, the initial configuration of the base stage is generated to insert the cannula through the trocar. Then, the robot arm is manipulated to actuate a cannula (Geuder G-34285, 23 gauge/0.64 mm) around the trocar in an RCM manner inside an eyeball phantom (VR-Eye by Simulated Ocular Surgery Ltd, London, inner radius 12.0∼12.5 mm). To enable direct 2D-3D mapping without optical distortion, the phantom's plastic cornea was removed for this study. Simultaneously, a microscope-mounted camera (Basler acA1920-155ucMED) captures the retinal status. The real-time microscope image is cropped to a 512x512 square

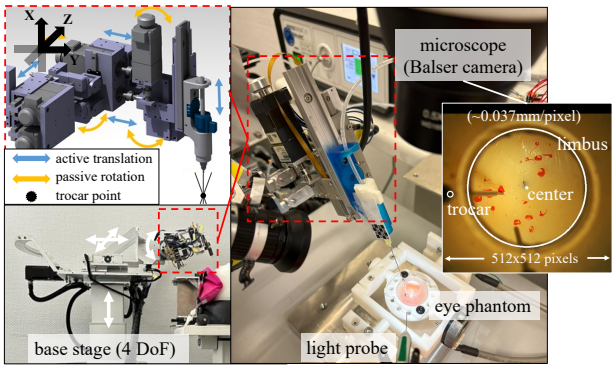

Fig. 7: Experiment setup consists of a ∼12mm-radius phantom and a TROST surgical system (a 5-DoF eye-surgery robot arm on a 4-DoF base stage).

area, with the eyeball center mapped to the image center pixel [255,255] and the mapping ratio $\sigma_{2d\to 3d} \approx 0.0366$ mm/pixel. Since our contribution is an intraocular visualization method that does not alter the low-level robotic tool control, we consider the experimental procedure on this commercial eye phantom to represent the core task in a real surgery.

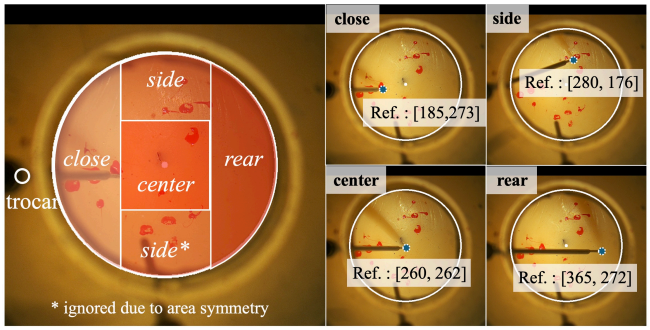

Fig. 8: Retina division into four parts with corresponding reference (touching) points for boundary generation.

We designed a structured experiment to systematically evaluate our visualization method under diverse geometric conditions. First, the microscope and eyeball were aligned, and a single trocar was fixed at image coordinates [23, 270] ([0.55, -8.50, 8.46] in the eyeball coordinate). With a fixed trocar (RCM) point and the same maximal working angle θ_{wv}^{max}, the shape and size of the projected working area on the curved retinal surface are highly dependent on the initial tool orientation. To test our method's robustness against these variations, we divided the visible retinal area (6mm radius) into four distinct sub-areas: close, side, center, and rear, which are located at varying distances and angles relative to the trocar (Fig. 8). For each of these four sub-areas, we performed a separate test. The robot's base stage was reconfigured to establish a unique reference touch point within that area, allowing us to generate and validate a different working area visualization. Due to symmetry, experiments for the side area were only conducted on the upper side. The specific parameters used to generate the working area boundaries in each case are listed in Table I.

TABLE I: Parameters of Working-Area Marking

Area	Ref. point (2D)	Ref. point (3D mapping result)
close	[185, 273]	[0.92, -3.57, -11.42]
side (up)	[280, 176]	[-4.03, 1.27, -11.23]
center	[260, 262]	[0.36, 0.25, -11.99]
rear	[365, 272]	[0.87, 0.51, -11.96]
$\theta_{wv}^{max} = 5°$, $\theta_{step} = 30°$, $N_{boundary} = 12$, $r_{eye} = 12.0$ mm		

The validation procedure was performed for each of the 12 boundary points (generated with θ_{step} =30°) in every sub-area. For each target point on the visualized boundary, the robot arm was commanded to move the cannula tip until it made physical contact with the inner phantom surface at that precise location. At the point of contact, we recorded the angles of the robot's two orthogonal rotational joints, t_2 and t_4, directly from the hardware encoders. Then, we calculate the cannula's true physical orientation $\vec{v}_{axis}^{now}$ using the robot's forward kinematics, as shown in Equation (10).

$$\vec{v}_{axis}^{now} = \mathbf{FK}(t_2, t_4) \cdot [0, 0, 1]^T \tag{10}$$

In this equation, $\mathbf{FK}(t_2, t_4)$ is the rotation matrix derived from the joint angles and $[0, 0, 1]^T$ is the unit vector representing the tool's axis in its local coordinate frame. Finally, the actual working angle, θ_{wv}^{real}, was calculated as the angle between this measured orientation, $\vec{v}_{axis}^{now}$, and the initial reference axis, $\vec{v}_{axis}^{ref}$. The visualization error for that point was then defined as the difference between the real angle and the theoretical maximum:

$$\theta_{wv}^{error} = \theta_{wv}^{real} - \theta_{wv}^{max} \tag{11}$$

A non-positive error ($\theta_{wv}^{error} \leqslant 0$) confirms the visualization covers the target point, while a positive error indicates the point is outside the accessible area and requires an extension of the conic working volume.

B. Results

The outcomes of the working-area visualization and the corresponding boundary-point accessibility tests are presented in Fig. 9 and Fig. 10, with quantitative metrics listed in Table II. Overall, the visualization proved to be a reliable predictor of the robot's physical workspace. Figure 9 displays the point-by-point angle error, θ_{wv}^{error}, for each of the 12 boundary points in all four subareas. A clear trend emerged across all test cases: boundary points located physically farther from the trocar (e.g., points 4-8) consistently showed more significant angle errors than those closer to the trocar (e.g., points 0, 1, 10, 11). Table II details the area coverage metrics for each configuration, showing that workspaces centered farther from the trocar (in the side, center, and rear areas) result in a larger projected retinal area.

A statistical summary of all 48 measured angle errors is provided in Fig. 10. Three of the four subareas (rear, close, and side) exhibited an average error smaller than 0.5°, while the center subarea showed a slightly larger, yet still small, average error of less than 1.0°. We classify the errors into two

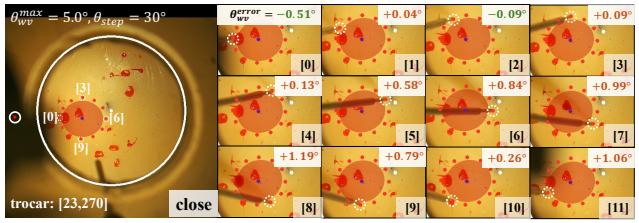

(a) Close Area: $\theta_{wv}^{error} \in$ [-0.51,1.19] deg.

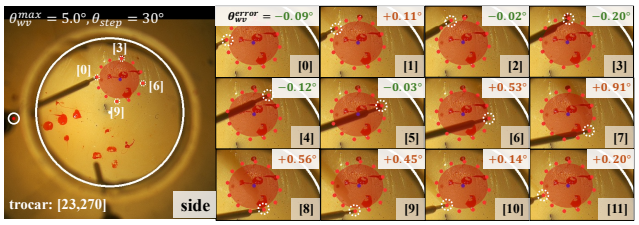

(b) Side (Up) Area: $\theta_{wv}^{error} \in$ [-0.20,0.91] deg.

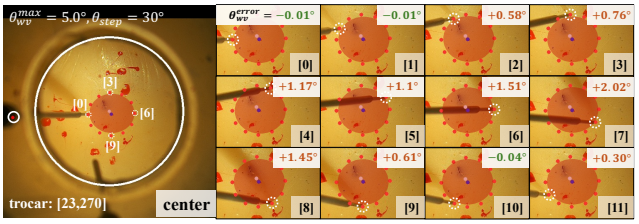

(c) Center Area: $\theta_{wv}^{error} \in$ [-0.04,2.02] deg.

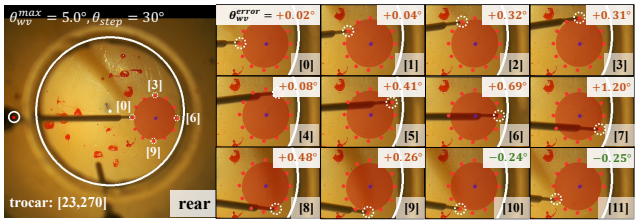

(d) Rear Area: $\theta_{wv}^{error} \in$ [-0.25,1.20] deg.

Fig. 9: The boundary-point visualization and their accessibility test in retinal subareas are presented. The angle error θ_{wv}^{error} of each point is given with "-"/"+" showing whether the desired boundary point is covered or not covered by the ideal θ_{wv}^{max}.

categories: "acceptable" errors ($0° \leq \theta_{wv}^{error} \leq 1.0°$), which could likely be compensated for by minor tissue deformation, and "out-ranged" errors ($\theta_{wv}^{error} > 1.0°$), which would require robot reconfiguration. Based on this classification, the proposed visualization correctly predicted accessibility for 83.3% of all tested points (25% were perfectly in range with $\leq 0°$ error, and 58.3% had an acceptable error).

V. DISCUSSION

The proposed method demonstrates a clinically acceptable level of precision in visualizing the robotic working volume, correctly predicting accessibility for over 83% of tested points. However, the accuracy of this visualization is fundamentally dependent on the fidelity of the 2D-3D mapping, which relies on a simplified projective model. This

TABLE II: Metrics of Retinal Area Coverage (Planar)

Section	Ref-RCM Dist (px)	Area (px^2)	Coverage
Close	162	8174	8.2%
Side	273	8688	8.7%
Center	237	8765	8.8%
Rear	342	8808	8.8%

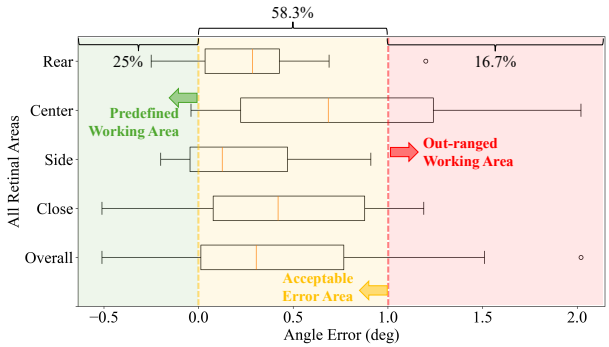

Fig. 10: Overall and case-specific error distribution compared with the predefined working volume angle.

section discusses the implications of this core assumption and outlines directions for future improvement.

The primary limitation of the current method is that it does not account for the accumulation of optical distortion from the eye [25] and microscope lens and segmentation errors. Our sensitivity analysis (Fig. 11) confirms this, showing that a small, 10-pixel error in trocar localization can lead to a substantial (10%) change in the calculated working area size. This finding helps explain a key trend from our main experiment (Fig. 10): the visualization error was consistently larger for boundary points farther from the trocar, where the geometric projection is most sensitive to small inaccuracies.

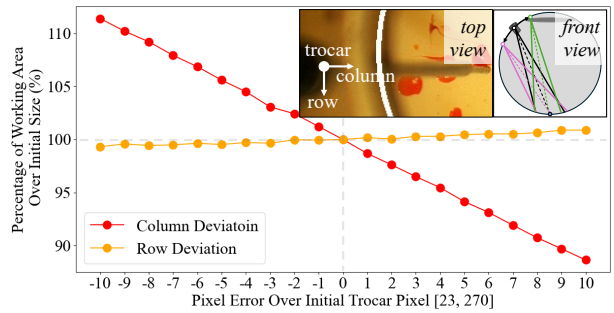

Fig. 11: Evaluation of the trocar error (col/row independently) over working-area sizes (p_{touch} =[255,255]).

Beyond optical distortion, our work relies on two other simplifying assumptions: a generic spherical eyeball model and a static eye. For eyeball modeling, patient-specific models could be created from preoperative diagnostic data, such as CT scans [26] or OCT volumes [27], to account for variations in eyeball shape. Moreover, a real-time eyeball pose tracking system would be required for clinical translation to dynamically update the visualization in response to patient movement. Finally, the symmetric conic model for the working volume could be replaced with more complex, robot-specific models to accommodate designs with asymmetric

capabilities. By addressing these challenges, the foundational framework presented here will be further enhanced into a robust tool for future clinical translation.

VI. CONCLUSIONS

This paper introduced and experimentally validated a novel method to provide surgeons with an intuitive visualization of the robotic tool's accessible workspace on the retina. By projecting the calculated working volume directly onto the microscope feed, our method allows surgeons to instantly verify if surgical targets are reachable and provides clear guidance for reconfiguring the robot to ensure complete coverage. However, the high accuracy of this visualization is fundamentally coupled to the fidelity of the underlying geometric models. Future work will therefore focus on integrating more sophisticated patient-specific and distortion-aware mapping techniques.

REFERENCES

[1] M. Roizenblatt, T. Edwards, and P. L. Gehlbach, "Robot-assisted vitreoretinal surgery: current perspectives," *Robotic Surgery: Research and Reviews*, vol. Volume 5, p. 1–11, Feb. 2018. [Online]. Available: http://dx.doi.org/10.2147/RSRR.S122301

[2] C. Irigoyen, A. Amenabar Alonso, J. Sanchez-Molina, M. Rodríguez-Hidalgo, A. Lara-López, and J. Ruiz-Ederra, "Subretinal injection techniques for retinal disease: A review," *Journal of Clinical Medicine*, vol. 11, no. 16, p. 4717, Aug. 2022. [Online]. Available: http://dx.doi.org/10.3390/jcm11164717

[3] N. A. Maierhofer, A.-M. Jablonka, H. Roodaki, M. A. Nasseri, A. Eslami, J. Klaas, C. P. Lohmann, M. Maier, and D. Zapp, "ioct-guided simulated subretinal injections: a comparison between manual and robot-assisted techniques in an ex-vivo porcine model," *Journal of Robotic Surgery*, vol. 17, no. 6, p. 2735–2742, Sept. 2023. [Online]. Available: http://dx.doi.org/10.1007/s11701-023-01699-4

[4] Q. Wang, Z. Li, C. Wang, Q. He, N. Xu, K. Yang, N. Li, M. Liu, H. Zhang, and L. Wang, "A novel robot-assisted subretinal injection system: preliminary validation in ex vivo porcine eyes," *Journal of Robotic Surgery*, vol. 19, no. 1, July 2025. [Online]. Available: http://dx.doi.org/10.1007/s11701-025-02521-z

[5] A. M. Bagci, M. Shahidi, R. Ansari, M. Blair, N. P. Blair, and R. Zelkha, "Thickness profiles of retinal layers by optical coherence tomography image segmentation," *American Journal of Ophthalmology*, vol. 146, no. 5, pp. 679–687.e1, Nov. 2008. [Online]. Available: http://dx.doi.org/10.1016/j.ajo.2008.06.010

[6] J. Cehajic-Kapetanovic, K. Xue, T. L. Edwards, T. C. Meenink, M. J. Beelen, G. J. Naus, M. D. de Smet, and R. E. MacLaren, "First-in-human robot-assisted subretinal drug delivery under local anesthesia," *American Journal of Ophthalmology*, vol. 237, pp. 104–113, 2022. [Online]. Available: https://www.sciencedirect.com/science/article/pii/S0002939421005924

[7] C. He, A. Ebrahimi, E. Yang, M. Urias, Y. Yang, P. Gehlbach, and I. Iordachita, "Towards bimanual vein cannulation: Preliminary study of a bimanual robotic system with a dual force constraint controller," in *2020 IEEE International Conference on Robotics and Automation (ICRA)*, 2020, pp. 4441–4447.

[8] A. Alikhani, S. Inagaki, B. Busam, K. Faridpooya, M. Maier, P. Gehlbach, I. Iordachita, N. Navab, M. A. Nasseri, D. Zapp, *et al.*, "Paros: Multi-component robotic system and an image-guided patient alignment for robot-assisted ophthalmic surgery," *IEEE Access*, 2025.

[9] K. Pachtrachai, F. Vasconcelos, G. Dwyer, S. Hailes, and D. Stoyanov, "Hand-eye calibration with a remote centre of motion," *IEEE Robotics and Automation Letters*, vol. 4, no. 4, pp. 3121–3128, 2019.

[10] Y. Koyama, M. M. Marinho, M. Mitsuishi, and K. Harada, "Autonomous coordinated control of the light guide for positioning in vitreoretinal surgery," *IEEE Transactions on Medical Robotics and Bionics*, vol. 4, no. 1, pp. 156–171, 2022.

[11] S. Inagaki, A. Alikhani, N. Navab, P. C. Issa, and M. A. Nasseri, "Pre-surgical planner for robot-assisted vitreoretinal surgery: Integrating eye posture, robot position and insertion point," 2025. [Online]. Available: https://arxiv.org/abs/2502.18230

[12] J. Yang, Z. Zhao, M. Maier, K. Huang, N. Navab, and M. Ali Nasseri, "Shadow-based 3d pose estimation of intraocular instrument using only 2d images," in *2024 IEEE International Conference on Robotics and Automation (ICRA)*, 2024, pp. 1323–1329.

[13] P. Hughes, C. Wilson, E. Semenova, and O. Olejnik, *Eye Structure and Physiological Functions*. CRC Press, Nov. 2006. [Online]. Available: http://dx.doi.org/10.1201/9780849332036.ch23

[14] S.-N. Yang, Y. Shi, and P.-O. Berggren, "The anterior chamber of the eye technology and its anatomical, optical, and immunological bases," *Physiological Reviews*, vol. 104, no. 3, p. 881–929, July 2024. [Online]. Available: http://dx.doi.org/10.1152/physrev.00024.2023

[15] R. Peter, S. Moreira, E. Tagliabue, M. Hillenbrand, R. G. Nunes, and F. Mathis-Ullrich, "Correction to: Stereo reconstruction from microscopic images for computer-assisted ophthalmic surgery," *International Journal of Computer Assisted Radiology and Surgery*, Nov. 2024. [Online]. Available: http://dx.doi.org/10.1007/s11548-024-03270-4

[16] M. Zhou, Q. Yu, K. Huang, S. Mahov, A. Eslami, M. Maier, C. P. Lohmann, N. Navab, D. Zapp, A. Knoll, and M. A. Nasseri, "Towards robotic-assisted subretinal injection: A hybrid parallel–serial robot system design and preliminary evaluation," *IEEE Transactions on Industrial Electronics*, vol. 67, no. 8, pp. 6617–6628, 2020.

[17] J. W. Kim, C. He, M. Urias, P. Gehlbach, G. D. Hager, I. Iordachita, and M. Kobilarov, "Autonomously navigating a surgical tool inside the eye by learning from demonstration," in *2020 IEEE International Conference on Robotics and Automation (ICRA)*, 2020, pp. 7351–7357.

[18] Y. Koyama, M. M. Marinho, and K. Harada, "Vitreoretinal surgical robotic system with autonomous orbital manipulation using vector-field inequalities," in *2023 IEEE International Conference on Robotics and Automation (ICRA)*. IEEE, May 2023, pp. 1–7.

[19] M. Zhou, Q. Yu, K. Huang, S. Mahov, A. Eslami, M. Maier, C. P. Lohmann, N. Navab, D. Zapp, A. Knoll, and M. A. Nasseri, "Towards robotic-assisted subretinal injection: A hybrid parallel–serial robot system design and preliminary evaluation," *IEEE Transactions on Industrial Electronics*, vol. 67, no. 8, pp. 6617–6628, 2020.

[20] S. Dehghani, M. Sommersperger, J. Yang, M. Salehi, B. Busam, K. Huang, P. Gehlbach, I. Iordachita, N. Navab, and M. A. Nasseri, "Colibridoc: an eye-in-hand autonomous trocar docking system," in *2022 International Conference on Robotics and Automation (ICRA)*, 2022, pp. 7717–7723.

[21] J. Yang, Z. Zhao, S. Shen, D. Zapp, M. Maier, K. Huang, N. Navab, and M. A. Nasseri, "Eyels: Shadow-guided instrument landing system for target approaching in robotic eye surgery," *IEEE Robotics and Automation Letters*, vol. 9, no. 4, pp. 3664–3671, 2024.

[22] T. Tayama, Y. Kurose, M. M. Marinho, Y. Koyama, K. Harada, S. Omata, F. Arai, K. Sugimoto, F. Araki, K. Totsuka, M. Takao, M. Aihara, and M. Mitsuishi, "Autonomous positioning of eye surgical robot using the tool shadow and kalman filtering," in *2018 40th Annual International Conference of the IEEE Engineering in Medicine and Biology Society (EMBC)*, 2018, pp. 1723–1726.

[23] N. Wang, X. Zhang, S. Bano, D. Stoyanov, H. Zhang, and A. Stilli, "Vision-based automatic control of a surgical robot for posterior segment ophthalmic surgery," *IEEE Transactions on Automation Science and Engineering*, vol. 22, pp. 6088–6099, 2025.

[24] G. Jocher, J. Qiu, and A. Chaurasia, "Ultralytics YOLO," Jan. 2023. [Online]. Available: https://github.com/ultralytics/ultralytics

[25] A. Kakehashi, "Improved fundus visualization during vitreous surgery using a combination of a prism contact lens and indirect ophthalmoscopy," *RETINAL Cases & Brief Reports*, vol. 1, no. 2, p. 101–103, 2007. [Online]. Available: http://dx.doi.org/10.1097/01.ICB.0000264812.68933.e5

[26] F. Ye, Y. Ji, Y. Chen, F. He, and X. Fan, "Orbital growth is associated with eyeball size: A study using ct-based three-dimensional techniques," *Current Eye Research*, vol. 47, no. 2, p. 317–324, Aug. 2021. [Online]. Available: http://dx.doi.org/10.1080/02713683.2021.1963784

[27] C. M. Bosch, C. Baumann, S. Dehghani, M. Sommersperger, N. Johannigmann-Malek, K. Kirchmair, M. Maier, and M. A. Nasseri, "A tool for high-resolution volumetric optical coherence tomography by compounding radial-and linear acquired b-scans using registration," *Sensors*, vol. 22, no. 3, 2022. [Online]. Available: https://www.mdpi.com/1424-8220/22/3/1135